AGU Word Manuscript Template

Global warming and equatorial Atlantic paleoceanographic changes during early Eocene carbon cycle perturbation V

Anne H. Kegel[1#], Chris D. Fokkema[1#], Henk Brinkhuis[1,2], Ursula Röhl[3], Thomas Westerhold[3], Claudia Agnini[4], Peter K. Bijl[1], Francien Peterse[1] and Appy Sluijs[1]

[1]Department of Earth Sciences, Faculty of Geoscience, Utrecht University, 3584CB Utrecht, The Netherlands

[2]Department of Ocean Systems research (OCS), Royal Netherlands Institute for Sea Research (NIOZ), 1790 AB Den Burg, The Netherlands.

[3]MARUM - Center for Marine Environmental Sciences, University of Bremen, Leobener Straße, 28359 Bremen, Germany

[4]Dipartimento di Geoscienze, Universita degli Studi di Padova, I-35131 Padova, Italy.

Corresponding author: Chris D. Fokkema (c.d.fokkema@uu.nl)

[#]Shared first authorship

Key Points:

- Equatorial sea surface and deep ocean warming marked early Eocene carbon isotope excursion V, implying it was a global warming event.
- A longer isotope recovery in organic compared to inorganic carbon suggests a contribution of older dissolved organic carbon at Site 959.
- Dinoflagellate cysts indicate a productive setting related to upwelling that commenced since the end of the Early Eocene Climatic Optimum.

Abstract

A series of transient global warming events ("hyperthermals") in the early Eocene is marked by massive environmental and carbon cycle change. Among these events, the impacts of the Paleocene Eocene Thermal Maximum (~56 Ma), Eocene Thermal Maximum 2 (~54 Ma) and Eocene Thermal Maximum 3 (~53 Ma) are relatively well documented, but much less is known on the many later hyperthermals that apparently occurred on orbital eccentricity maxima until at least the end of the Early Eocene Climatic Optimum (EECO; ~53–49 Ma). Here, at Ocean Drilling Program (ODP) Site 959 (Equatorial Atlantic Ocean), we report a large negative carbon isotope excursion (CIE) in both organic and carbonate substrates that we correlate to the "V" event *sensu* Lauretano et al. (2016) (or C22nH1 *sensu* Sexton et al. (2011)) at ~49.7 Ma, following combined bio- and chemostratigraphic

constraints. Through TEX_{86} paleothermometry, we reconstruct a sea surface temperature rise of 1.1–1.9 ºC associated with this CIE, which, combined with evidence for warming from the deep sea, implies that this event indeed represents a transient global-scale warming episode like the earlier hyperthermals. Organic walled dinoflagellate cyst assemblages indicate a productive paleoceanographic background setting, likely through regional upwelling, which alternated with episodes of stratification. Warming reconstructed across V at Site 959 is relatively similar to the higher-latitude-derived deep ocean reconstructions. However, the presence of upwelling and its variable intensity across the event compromises the use of the reconstructed warming as an estimate for the complete tropical band.

1. Introduction

Persistent deep ocean warming during the late Paleocene and early Eocene climaxed at the end of the Early Eocene Climatic Optimum (EECO; ~53–49 Ma) (Shackleton, 1986; Westerhold et al., 2020). This trend is mimicked by sea surface temperature (SST) reconstructions in both low and middle, and high latitudes, indicating that they represent global mean surface temperature (GMST) variability (e.g., Bijl et al., 2009; Hollis et al., 2012; Cramwinckel et al., 2018; Gaskell et al., 2022). During the EECO, GMSTs were approximately 10–16 ºC elevated relative to pre-industrial temperatures (Inglis et al., 2020) and atmospheric pCO_2 exceeded 1000 ppmv (Anagnostou et al., 2020).

Superimposed on this long-term trend occur approximately 20 transient negative stable carbon ($\delta^{13}C$) isotope excursions (CIEs) in the ocean-atmosphere system (Kennett and Stott, 1991; Cramer et al., 2003; Lourens et al., 2005; Agnini et al., 2009; Sexton et al., 2011; Littler et al., 2014; Kirtland Turner et al., 2014; Frieling et al., 2018; Lauretano et al., 2018). These transient CIEs and associated deep ocean carbonate dissolution horizons likely reflect the rapid and massive injection of ^{13}C-depleted carbon from outside the global exogenic carbon reservoir pool into the ocean-atmosphere system (Dickens et al., 1995, 1997). It is demonstrated that most or all of these events are paced by eccentricity cycles of ~100- and ~405-kyrs (Cramer et al., 2003; Lourens et al., 2005; Galeotti et al., 2010; Zachos et al., 2010; Littler et al., 2014; Lauretano et al., 2016; Laurin et al., 2016; Westerhold et al., 2017, 2018; Piedrahita et al., 2022). This view is recently strengthened by a recorded loss in resilience in climate-carbon cycle dynamics leading up to the events (Setty et al., 2023). The coeval negative excursions in benthic foraminiferal oxygen isotope ratios ($\delta^{18}O$) are interpreted to reflect deep ocean warming (Kennett and Stott, 1991; Lourens et al., 2005; Lauretano et al., 2018). SST proxy records indicate that at least a great part of these events indeed represent global warming events (Lourens et al., 2005; Sluijs et al., 2009; Dunkley Jones et al., 2013; Frieling et al., 2018; Fokkema et al., 2023) and can therefore be termed ‘hyperthermals’ (Thomas and Zachos, 2000). However, the exact driving mechanisms and carbon sources are still under debate (e.g., Frieling et al., 2019). Potential external carbon sources can include (a combination of) methane hydrates and terrestrial organic carbon (Dickens et al., 1995; Kurtz et al., 2003; DeConto et al., 2012). Volcanic sources may have contributed to carbon injection during the largest hyperthermal, the Paleocene-Eocene Thermal Maximum (PETM; ~56 Ma; e.g., Svensen et al., 2004; Frieling et al., 2019; Berndt et al., 2023).

The PETM is associated with massive environmental and concomitant biotic change on land and in the ocean (Sluijs et al., 2007; McInerney and Wing, 2011; Hupp et al., 2022). Some of the subsequent lesser hyperthermals are regionally associated with biotic changes as well, notably Eocene Thermal Maximum 2, and Eocene Thermal Maximum 3, but others, where documented, show little to no change (Agnini et al., 2009; Sluijs et al., 2009; Gibbs et al., 2012; Willard et al., 2019; Rush et al., 2023). In contrast, it has been proposed that in some tropical regions during the PETM, high-resolution fossil organic walled dinoflagellate cyst (dinocyst) and planktic foraminifer assemblages suggest the disappearance of eukaryotic plankton because of heat stress, when warming

led to temperatures near thermo-physiological limits, or the rate of warming resulted in reduced prevalence and biodiversity (Aze et al., 2014; Frieling et al., 2017, 2018).

So far, most studies focused on the early set of hyperthermals, whereas the events that occurred during the later part of the EECO received much less attention (Sexton et al., 2011; Kirtland Turner et al., 2014; Westerhold et al., 2017, 2018). Consequently, while for a series of the earlier hyperthermals (PETM–L2, ~56–52.4 Ma) surface ocean warming has been reconstructed in multiple regions including the tropics (Sluijs et al., 2009; Frieling et al., 2017, 2018; Fokkema et al., 2023), evidence for warming of hyperthermals during the later part of the EECO (~52–49 Ma) is limited to negative excursions in benthic foraminiferal $\delta^{18}O$ (Westerhold et al., 2018), that presumably reflects Southern Ocean SST variability (Hollis et al., 2012; Zhang et al., 2022). In addition, to our knowledge, no studies of biotic change have been carried out for these later perturbations.

Therefore, here we aim to evaluate temperature and ecological variability across the later part of the EECO in sediments recovered at Ocean Drilling Program (ODP) Site 959, located in the Equatorial Atlantic (Fig. 1). Previous Eocene reconstructions on Site 959 using TEX_{86} (TetraEther indeX of tetraethers consisting of 86 carbon atoms) paleothermometry have demonstrated that the PETM was associated with ~3 ºC warming, and hyperthermals I1–L2 with ~1–1.5 ºC from baseline temperatures exceeding 33 ºC (Frieling et al., 2019; Fokkema et al., 2023). We follow up on this work by searching for CIEs using stable carbon isotope analyses on a late-EECO interval of Site 959. We will constrain the chronostratigraphy using the available biostratigraphic data and identify hyperthermal related variability in the record. Then we assess environmental and biotic changes over the interval using TEX_{86} and palynological associations.

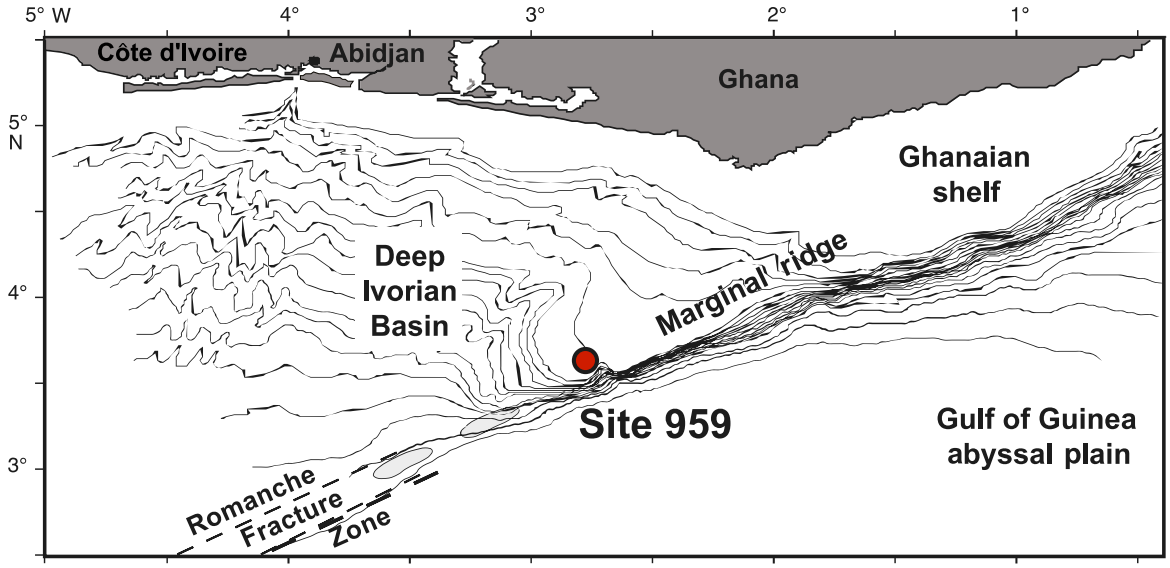

Figure 1. Present day location of ODP Site 959 in the eastern equatorial Atlantic Ocean. Map adapted from Mascle et al. (1996).

2. Material and methods

2.1 Ocean Drilling Program Site 959

ODP Leg 159 Site 959 (3.62760º N, 2.735817º W) is located ~140 km offshore of Ghana in the eastern equatorial Atlantic Ocean at a depth of 2100 m on the northern slope of the Côte d'Ivoire-Ghana Marginal Ridge, which divides the Deep Ivorian Basin from the abyssal plain of the Gulf of Guinea (Mascle et al., 1996) (Fig. 1). Site 959 has accumulated sediments with ample organic matter since the Late Cretaceous (Wagner, 2002), which has allowed for low latitude paleoclimate reconstructions by lipid biomarkers and organic walled dinoflagellate cysts (dinocysts) throughout the Cenozoic Era (e.g., Cramwinckel et al., 2018; van der Weijst et al., 2022). The lower Eocene sediments, consisting of clay-bearing chalks and porcellanites (Mascle et al., 1996), were deposited at a paleolatitude of ~9° S (*http://paleolatitude.org, model version 2.1*; (van Hinsbergen et al., 2015); using the paleomagnetic reference frame of Torsvik et al. (2012)). An open marine depositional environment during the early Eocene was inferred by previous work based on the (near) absence of terrestrial palynomorphs an dominance of dinocyst taxa typical for outer shelf to open marine environments (Fokkema et al., 2023). The appearance of heterotrophic dinocysts and increased total organic carbon (TOC) content around the end of the early Eocene (~49 Ma) suggests the onset, or intensification of upwelling around that time (Cramwinckel et al., 2018; Fokkema et al., 2023).

2.2 Stratigraphic framework

The PETM and CIEs I1 to L2 were previously identified in Hole D Cores 42R (Frieling et al., 2018) and 39R (Fokkema et al., 2023; Fig. 2). Core 38R had very poor recovery (10 %, Mascle et al., 1996). Therefore, our search for late EECO CIEs focuses on Core 37R, which has reasonable recovery (51.8 %, Mascle et al., 1996) (Fig. 2). Incomplete recovery around the studied interval complicates the construction of a reliable stratigraphic framework. However, the base of calcareous nannofossil *Discoaster sublodoensis* in Core 37R at 755.11±0.04 mbsf (Fokkema et al., 2023) provides important constraints. This event is generally considered a problematic biohorizon, due to its relative proneness to diagenetic overgrowth, its sporadic occurrences in the lower part of its range (Backman, 1986), its relatively recently improved taxonomy (Agnini et al., 2006) and its inconsistent position at Walvis Ridge ODP Sites 1265 and 1263 (Westerhold et al., 2017). Nevertheless, the use of a consistent taxonomy and the standardization of a semi quantitative counting result in a very consistent position of this event between astronomically tuned ODP Sites 1265 (Walvis Ridge, South Atlantic) and Site 1258 (Demerara Rise, equatorial Atlantic), where it is reported in the base of magnetochron C22n, between the V (49.685 Ma; C22nH1) and W (49.585 Ma; C22nH2) CIEs (Westerhold et al., 2017). The offset observed between Site 1263 and 1265 is potentially caused by core disturbance of this interval at Site 1263 (Westerhold et al., 2017). Therefore, the available data support the hypothesis that the base of *D. sublodoensis* is indeed positioned between the V and W CIEs. The calculated age of this event at Sites 1265 and 1258 is also consistent with the tuned age of this biohorizon at the Newfoundland Ridge International Ocean Discovery Program (IODP) Site U1410, although that site lacks paleomagnetic data in that interval (Cappelli et al., 2019). Moreover, the position between V and W agrees with unpublished observations of the base of *D. sublodoensis* datum from the low-latitude Pacific ODP Site 1209 (C. Agnini, personal observation, 2023). Collectively, we might expect to find CIEs V and/or W close to this bioevent.

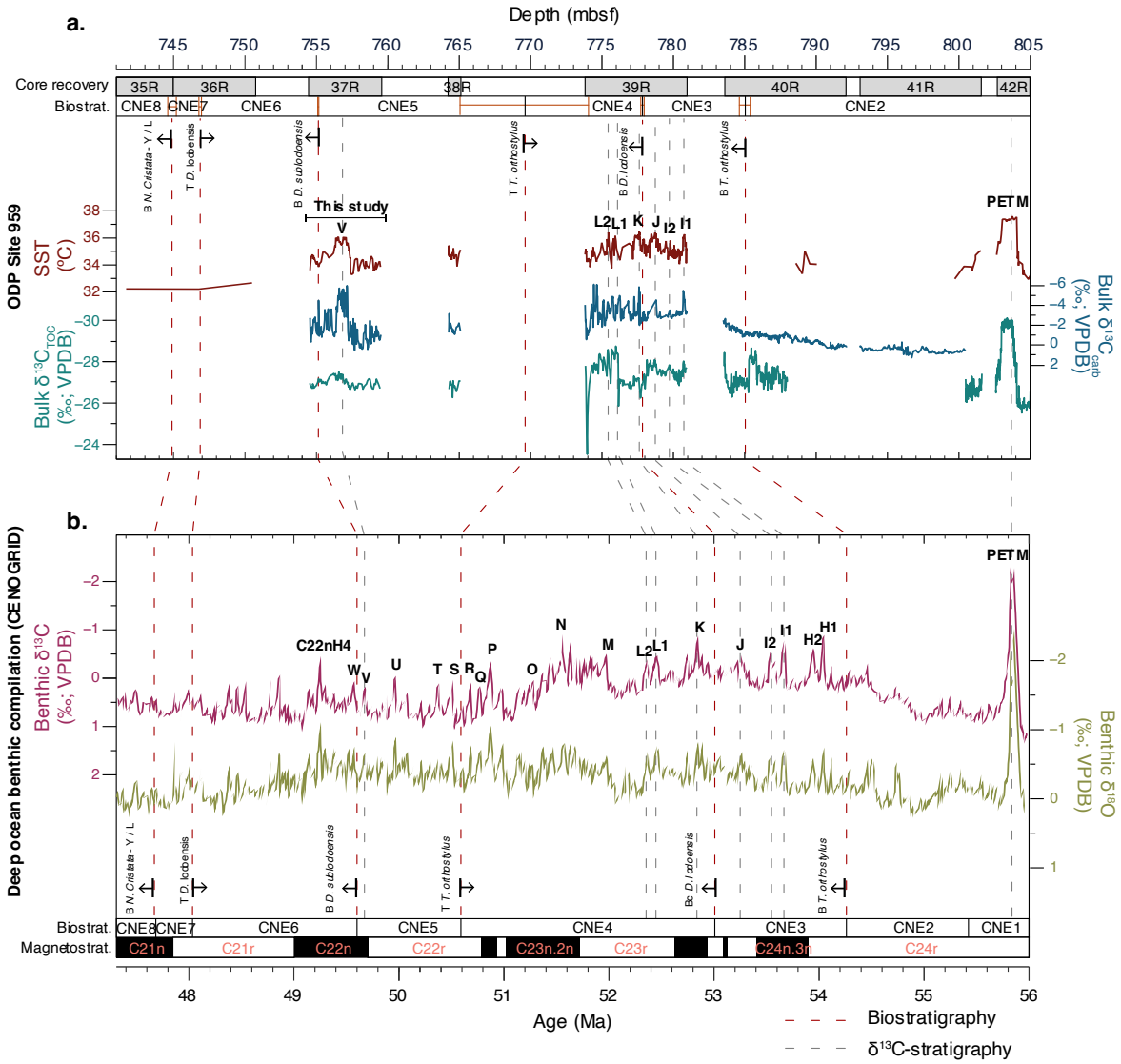

Figure 2. Stratigraphic correlation of Site 959 to a global deep ocean benthic compilation. (**a**) Site 959 data (TEX_{86}-based SST, bulk organic and carbonate $\delta^{13}C$, calcareous nannofossil biostratigraphy), including newly generated data for Core 37R and previously published data (Frieling et al., 2018, 2019; Cramwinckel et al., 2018; Fokkema et al., 2023). (**b**) benthic foraminiferal $\delta^{13}C$ and $\delta^{18}O$ from the CENOGRID compilation (Westerhold et al., 2020). The dashed lines mark the correlations based on calcareous nannofossils (red) and CIEs (grey). The calcareous nannofossil biostratigraphic zonation (CNE zones) follows definitions by Agnini et al. (2014), and the ages are the astronomically calibrated by Westerhold et al. (2017).

2.3 Methods

For this study, we continuously sampled the working halves of Hole 959D, Core 37R (759.5–754.5 mbsf) at 2 cm resolution at the Bremen Core Repository of the IODP. All samples were freeze-dried. Selections of samples were analyzed for magnetic susceptibility, bulk carbonate stable carbon and oxygen isotope ratios, bulk organic carbon isotope ratios, biomarkers, and palynology. Archive halves were subject to X-Ray Fluorescence (XRF) scanning.

172 2.3.1 Color Reflectance

173 Total color reflectance data was generated from the original sediment core images (Mascle et
174 al., 1996) following the methodology described by Zeeden et al. (2015). Images were prepared by
175 deleting cracks, drilling mud and other unconformities, and data was generated at 1-cm resolution
176 using the R-script by Kocken (2022).

177 2.3.2 Bulk magnetic susceptibility

178 For bulk magnetic susceptibility (MS) measurements, samples were crushed to ~0.5 cm large
179 pieces and weighed. MS was measured with a MFK1-FA on 212 samples at Utrecht University. Each
180 measurement was repeated at least thrice. Analytical uncertainty was smaller than 5.3×10^{-10} χ.

181 2.3.3 XRF scanning

182 XRF Core Scanner data were collected in 2009 every 1 cm down-core over a 1.2 cm^2 area
183 with a down-core slit size of 10 mm using generator settings of 10 kV, a current of 0.2 mA, and a
184 sampling time of 30 seconds directly at the split core surface of the archive half with XRF Core
185 Scanner III (AVAATECH Serial No. 12) at the MARUM - University of Bremen. The split core
186 surface was covered with a 4 µm thin SPEXCerti Prep Ultralene1 foil to avoid contamination of the
187 XRF measurement unit and desiccation of the sediment. The here reported data have been acquired
188 by a Canberra X-PIPS Detector (Model SXP 5C–200–1500) with 200eV X-ray resolution, the
189 Canberra Digital Spectrum Analyzer DAS 1000 and an Oxford Instruments 100W Neptune X-ray
190 tube with rhodium (Rh) target material. Raw data spectra were processed by the analysis of X-ray
191 spectra by Iterative Least square software (WIN AXIL) package from Canberra Eurisys.

192 2.3.4 Isotope measurements

193 Stable carbon and oxygen isotope ratios of bulk carbonate ($\delta^{13}C_{carb}$ and $\delta^{18}O_{carb}$, respectively)
194 were measured on powdered samples using a Thermo Finnigan GasBench II system coupled to a
195 Thermo Delta-V isotope ratio mass spectrometer (IRMS) at Utrecht University. Results were
196 calibrated to delta values relative to the Vienna Pee Dee Belemnite (VPDB) using an in-house
197 carbonate standard "NAXOS" ($\delta^{13}C$ = 2.08 ‰; $\delta^{18}O$ = -6.83 ‰) and the international carbonate
198 standard IAEA-CO-1. Analytical precision, based on repeated measurements of NAXOS, were better
199 than 0.11 ‰ for $\delta^{18}O_{carb}$ and 0.05 ‰ for $\delta^{13}C_{carb}$ (1σ). For 15 samples that required relatively large
200 amounts of sediment (>1000 µg) due to low carbonate content, analytical uncertainty increased up to
201 1 ‰ due to H_2S formation.

202 For bulk organic carbon isotope ratios ($\delta^{13}C_{TOC}$), approximately 0.3 gram per sample was
203 powdered, and treated with 25 mL HCl to dissolve the carbonates. Samples were crushed after
204 drying and analyzed on a Thermo Scientific Flash IRMS Elemental Analyzer coupled to a Thermo
205 Scientific Delta V Advantage isotope ratio mass spectrometer. Standard bracketing using the in-
206 house standard nicotinamide ($\delta^{13}C$ = -33.08‰) allowed for calibration of delta values relative to the
207 VPDB. Analytical precision, based on repeated measurements of the nicotinamide standard, were
208 smaller than 0.05 ‰ (1σ).

209 2.3.5 Total organic carbon content and carbonate weight percentage

210 The $CaCO_3$ content ($CaCO_3$wt%) was approximated by two independent methods; the first
211 estimation was based on the weight loss after decalcification with HCl, here-after referred to as
212 "$CaCO_3wt\%_{wl}$ (see section 2.3.4). This method presumably slightly overestimates the $CaCO_3$ content
213 due to removal of additional material (e.g., salts). In the second method, the $CaCO_3$wt% was
214 approximated based on the relation between the mass spectrometer m/z 44 signal intensity and mass
215 of the weighted sediment sample, in comparison to that of the pure carbonate standards (same

approach as described in Fokkema et al., (2022)) here-after referred to as "$CaCO_3wt\%_{ms}$. The precision was better than 9.5% (1σ) based on the carbonate standards.

The weight percentage of total organic carbon content (TOCwt%) was measured on the EA during $\delta^{13}C_{TOC}$ analysis. Analytical precision, based on repeated measurements of the nicotinamide standard, was better than 0.05% (1σ).

2.3.6 GDGT analysis

For 92 samples, a subsample of ~4–16 g was powdered for the analysis of glycerol dialkyl glycerol tetraethers (GDGTs). Lipids were extracted with a mixture of dichloromethane (DCM) and MeOH (9:1, v/v) using a Milestone Ethos X Microwave extraction system (70 ºC; 50 min). An internal standard (99 ng of C_{46} GTGT) was added to allow for quantitative assessment of GDGT concentrations. Subsequently, solvent mixtures of hexane:DCM (9:1), hexane:DCM (1:1) and methanol:DCM (1:1) were used to respectively separate the total lipid extract into apolar, ketone and polar fractions over an activated Al_2O_3 column. The polar fractions, containing the GDGTs, were dried under a gentle N_2 stream, redissolved in hexane:isopropanol (99:1) and filtered through a 0.45 µm polytetrafluorethylene filter, after which they were measured on an Agilent 1290 ultra-High Performance Liquid Chromatography (UHPLC) coupled to a Agilent 6135 Mass Spectrometer (MS), following the methodology as described by Hopmans et al. (2016). GDGTs were identified by detecting their $[M+H]^+$ ions in selected ion monitoring mode. Quantification was achieved by peak area integration and comparing that with the area of the internal standard, assuming that the response of the MS was similar for all compounds. A minimum signal-to-noise ratio of >3 was maintained as detection limit.

GDGT distributions were first tested for non-thermal controls on the TEX_{86} using various published ratios and indices by applying the R script of Bijl et al. (2021), resulting in exclusion of two samples (Supplementary Fig. S1). TEX_{86} values were translated to temperatures using a SST calibration (TEX_{86}^H; Kim et al., 2010) and, because sedimentary GDGTs most likely derive from just below the mixed layer (Massana et al., 2000; Taylor et al., 2013; Rattanasriampaipong et al., 2022), also with a subsurface temperature calibration (SubT) that targets the layer between 100 and 250 m water depth ($SubT_{100\text{-}250m}$; Ho and Laepple, 2016). To properly assess SST variability, we use the range of variability in SST and SubT-calibrated TEX_{86} records to cover the plausible range of depth-depended TEX_{86}-temperature slopes in the modern system (see Fokkema et al. (2023)). Analytical precision, based on repeated integrations of the standard (n = 4), were smaller than 0.0015 TEX_{86} values, which translates to 0.06 ℃ following the TEX_{86}^H calibration in the range of TEX_{86} values encountered.

2.3.7 Palynology

Forty-one samples were crushed to ~5 mm size pieces and prepared in the Palynology Lab at Utrecht University, using standard methods (e.g., Cramwinckel et al., (2018)). In short, samples were treated with HCl and HF and residues were sieved over 250- and 15-µm sieves. The addition of a known number of *Lycopodium clavatum* spores prior to processing provides for quantitative assessment (Stockmarr, 1972). Microscope slides were prepared using glycerine jelly. Dinocysts were classified at genus and if possible, at species level, using the taxonomy of that cited in Williams et al. (2017). Taxa were grouped based on inferred ecological niches, following modern (Zonneveld et al., 2013; Thöle et al., 2023) and Paleogene distributions and affinities (Brinkhuis, 1994; Pross and Brinkhuis, 2005; Sluijs and Brinkhuis, 2009; Frieling and Sluijs, 2018).

3. Results

3.1 Bulk carbonate and bulk organic isotopic compositions

3.1.1 Carbon isotope excursion "V"

We record a significant CIE in the $\delta^{13}C_{carb}$ and $\delta^{13}C_{TOC}$ data between ~757.2–756.3 mbsf (Figs. 2, 3), with magnitudes of 3.4 ‰ and 0.6 ‰, respectively. The timing of recovery to background values differs between $\delta^{13}C_{carb}$ and $\delta^{13}C_{TOC}$, the rise in $\delta^{13}C_{carb}$ at 756.36 mbsf precedes that of the $\delta^{13}C_{TOC}$ by ~55 cm. The $\delta^{18}O_{carb}$ data exhibits overall low values (mean = -4.7 ‰) that drop to values as low as -7.1 ‰ during the CIE (Supplementary Fig. S1). Although this negative oxygen isotope excursion might support the presence of a hyperthermal, such low values may also point to secondary overprint of the $\delta^{18}O$ signals (Schrag et al., 1995). Therefore, we do not further interpret $\delta^{18}O_{carb}$ as a paleoclimatic proxy indicator. Collectively, however, this CIE stands out significantly relative to background values suggesting the presence of a globally recorded CIE. The CIE occurs just below the base of *D. sublodoensis*, implying that it most likely represents the "V" CIE at 49.7 Ma (Lauretano et al., 2016) (also termed "C22nH1"; Sexton et al., 2011) (see section 2.2; Fig. 2).

3.1.2 Background $\delta^{13}C$ variability

The $\delta^{13}C_{carb}$ ranges between ~-2 and 0 ‰ from the base of Core 37R up to the V event (759.5–757.2 mbsf). Above the event (<756.3 mbsf), $\delta^{13}C_{carb}$ values recover to average values between ~-3 and -1 ‰ (Fig. 3). The $\delta^{13}C_{TOC}$ data shows ~50 cm background variability between -26.7 ‰ and -27.2 ‰ surrounding V. Within the CIE, values vary between -27.5 and -27.1 ‰.

3.2 Sediment composition

3.2.1 Core picture and sediment color

Site 959D Core 37R is characterized by prominent variations in sediment color, ranging from dark brown to light grey (Fig. 3). Across the complete core, the darker and lighter intervals alternate on submeter scale. An extended dark horizon marks the V event in the middle of the core between 757.2 to 756.3 mbsf, and relatively light-colored sediments mark the lower part of the section. One occurrence of a black chert at ~755.4 mbsf stands out in the core picture.

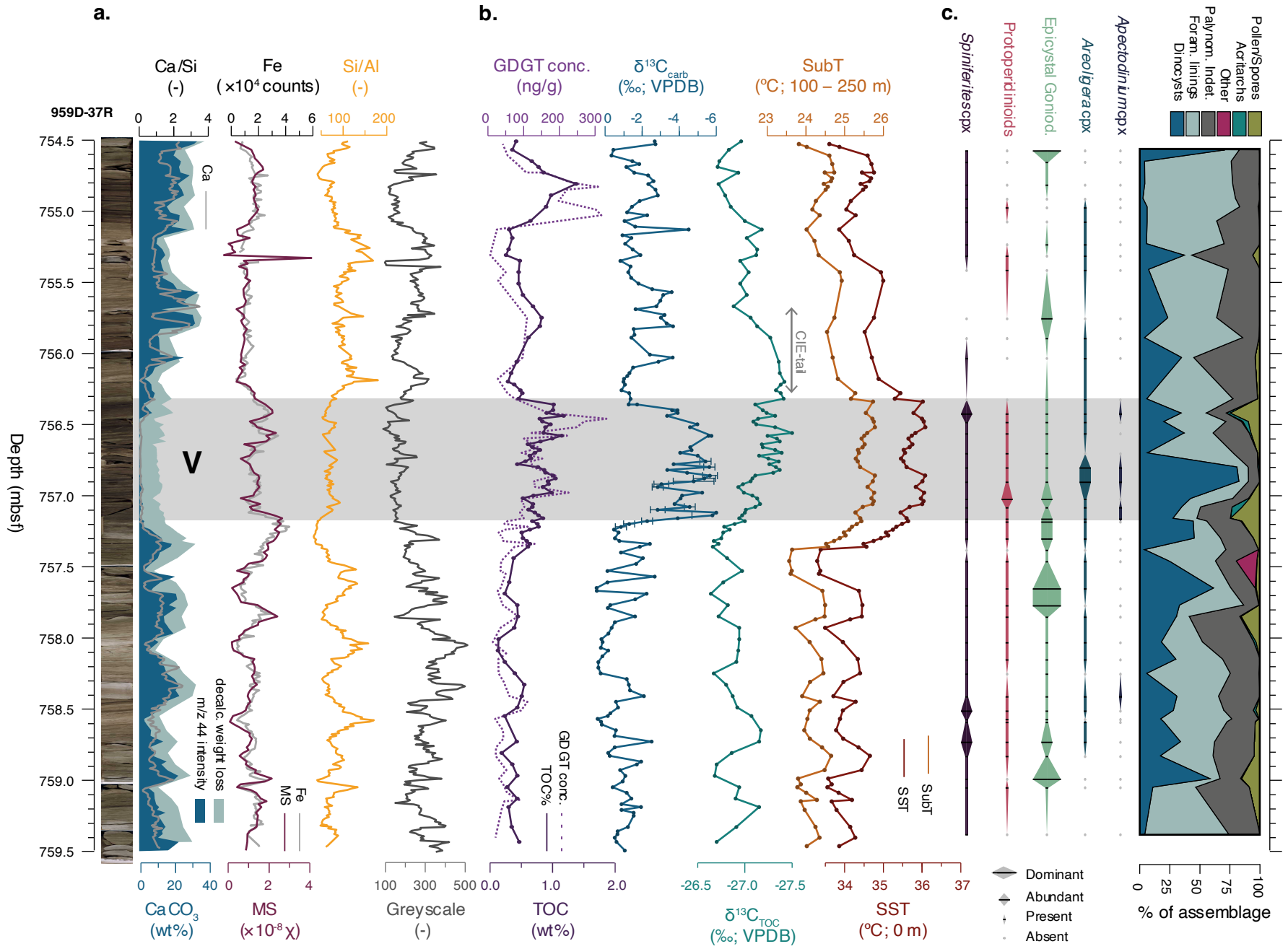
a.
b.
c.
959D-37R
Depth (mbsf)
754.5
755.0
755.5
756.0
756.5
757.0
757.5
758.0
758.5
759.0
759.5
V
Ca/Si (-)
Fe (×10⁴ counts)
Si/Al (-)
Ca
decalc. weight loss
m/z 44 intensity
Fe
MS
Ca CO3 (wt%)
MS (×10⁻⁸ χ)
Greyscale (-)
GDGT conc. (ng/g)
δ13Ccarb (‰; VPDB)
SubT (°C; 100 – 250 m)
CIE-tail
GDGT conc.
TOC%
SubT
SST
TOC (wt%)
δ13CTOC (‰; VPDB)
SST (°C; 0 m)
Spiniferites cpx
Protoperidinioids
Epicystal Goniod.
Areoligera cpx
Apectodinium cpx
Pollen/Spores
Acritarchs
Other Palynom. Indet.
Foram. linings
Dinocysts
% of assemblage
Dominant
Abundant
Present
Absent

Figure 3. Downcore analysis results for Site 959D Core 37R. (**a**) Calcareous nannofossil biostratigraphic zonation (data from Fokkema et al. (2023); zonation definitions follows Agnini et al. (2014)). Two methods for $CaCO_3$wt% (dark and light blue areas, see section 2.3.5) and Ca/Si (grey line), bulk magnetic susceptibility (MS) and XRF-based Fe counts, Si/Al, Greyscale. (**b**) TOCwt% and GDGT concentrations (dotted line), bulk carbonate $\delta^{13}C$, total organic $\delta^{13}C$, TEX_{86}-based SubT (orange, following the $SubT_{100\text{-}250m}$ calibration; Ho and Laepple, 2016) and SST (red, following the TEX_{86}^{H} calibration; Kim et al. 2010). (**c**) Palynology results with semi-quantitative dinocyst assemblages and the relative abundances of constituents that make up the complete palynomorph assemblage. Dark grey band indicates the CIE horizon.

3.2.2 $CaCO_3$ and organic carbon content

The two independent $CaCO_3$wt% proxies (light and dark blue areas in Fig. 3a) correlate well (R^2=0.87; $p < 0.001$), but the decalcification-weight-loss method yields 5–10 wt% higher values (Supplementary Fig. S1), presumably due to the loss of non-$CaCO_3$ components during HCl treatment. The $CaCO_3$wt% (m/z 44 method) displays a continuous ~50 cm variability across the bottom half of the core, ranging between ~2–24 % and strongly declines to negligible amounts during the V event. Above this horizon, $CaCO_3$wt% rises to values of approximately 10 % higher than the lower interval, varying between 10–34 % on meter scale.

The TOCwt% varies in-phase with $CaCO_3$wt% in the top and bottom part of the interval, ranging between 0.2–0.6% in ~50 cm intervals in the bottom halve of the core. In the dark colored interval marking V, TOCwt% rises to higher values up to 1.2%. Above, the TOCwt% remains elevated compared to the base of the section and reaches two maxima at 755.75 and 754.75 mbsf, with values of 0.85 and 1.4 %, respectively.

3.2.3 Magnetic Susceptibility

The MS values (Fig. 3a) range between -3.7×10^{-9}–3.9×10^{-8} χ. Overall variability in the MS record corresponds to that of TOCwt%: showing a continuous ~50 cm variability from the base of the section to 756.36 mbsf, with relatively higher values during V. The ~1m-scale variability above the V event to the top of the section is relatively dampened. Interestingly, one high MS peak coincides with the bottom of the identified black chert, immediately followed by slightly negative MS.

3.2.4 X-Ray Fluorescence (XRF)

Ca and Si compose the bulk signal intensity of the XRF scan. Ca significantly covariates with the $CaCO_3wt\%_{ms}$ ($R^2 = 0.82$; $p < 0.001$) and $CaCO_3wt\%_{wl}$ ($R^2 = 0.73$, $p < 0.001$) (Supplementary Fig. S1). For most of the record, Si and Ca display a strong anticorrelation across regular ~50-cm-scale alternations, whereas both elements decline during V (757.4–756.4 mbsf). Interestingly, the regular occurring maxima of Si and Ca are both in the lighter core intervals. Furthermore, Fe correlates strongly with the MS, Al and K (Supplementary Fig. S1**)**, representatives of the terrestrially derived clay component.

3.3 TEX_{86} paleothermometry

Concentrations of isoprenoid GDGTs range between 6–332 ng/g throughout the core. All isoprenoid GDGTs relevant for TEX_{86} paleothermometry were above detection limit in all

samples. An average GDGT-2/GDGT-3 ratio of 3.7 indicates predominant GDGT export origin from the upper top 200 meters of the ocean water column (Taylor et al., 2013; Hurley et al., 2018; van der Weijst et al., 2022; Rattanasriampaipong et al., 2022). There is no clear correlation between the TEX_{86} and the GDGT-2/GDGT-3 ratio ($R^2 = 0.05$; $p = 0.026$). Branched GDGTs are absent or only present in low concentrations, hence the branched and isoprenoid tetraether (BIT) index that can indicate potential GDGT inputs from the terrestrial realm (Hopmans et al., 2004) reflects consistently very low values (<0.01), characteristic for open marine settings. Two samples show large (>0.3) deviations from the modern Ring Index-TEX_{86} relationship (Δ-RI; Zhang et al., 2016) indicating a possible non-thermal overprint on the temperature signal and were discarded (Supplementary Fig. S2).

Reconstructed temperatures change from background SSTs varying between 33.3–34.5 ºC (SubT = 23.6–24.5 ºC) rising to values varying between 35.5–36.1 ºC (SubT = 25.3–25.8 ºC) during the V event, reflecting an averaged warming of 1.1 (SubT)–1.9 ºC (SST) (Fig. 3b). The background SSTs of ~34 ºC are close to two previous data points from Cramwinckel et al. (2018) for this interval at Site 959. After the CIE, background temperatures are on average ~0.5 ºC higher than before. Interestingly, the onset of warming leads the onset of the CIE by ~10 cm. In addition, the warming includes two warm phases with temperatures up to ~36 ºC, separated by a 0.5 °C cooling at the level where carbon isotope ratios reach minimum levels. Finally, throughout the studied interval, TEX_{86} shows a continuous ~50 cm variability, which is dampened during the hyperthermal.

3.4 Palynology

The palynological associations are mainly composed of dinocysts and remains of the organic inner-wall 'linings' of benthic foraminifera (Fig. 3c). The contribution of terrestrial elements, (notably various types of pollen and spores) is generally low, with larger numbers, occasionally up to ~25% in certain samples. These intervals of higher proportions of terrestrial palynomorphs coincide with higher MS and Fe values, and darker sediment color. Unfortunately, the overall poor preservation of dinocysts prohibits the confident and complete quantification of the dinocyst assemblages for most analyzed samples; because of large number of unidentifiable (fragments of) dinocysts, only 10 samples have more than 30 specimens that could be identified at family or genus level. Therefore, we discuss the dinocyst assemblages only in terms of broad qualitative and semi-quantitative results.

We do record the near-continuous occurrence of dinocysts that belong to the ecological groupings of *Areoligera*, *Spiniferites*, Protoperidinoids, Goniodomideae with an epicystal archeopyle (epicystal Goniodomids) and a rest group of Gonyaulacoids with a precingular archeopyle (cf. Frieling and Sluijs, 2018). In addition, many of the unidentified dinocysts represent skolochorate dinocysts probably of Gonyaulacoid affinity. The occurring Protoperidinoid cysts, notably *Selenopemphix* spp. and *Lejeunecysta* spp., represent obligate heterotrophic dinoflagellates today (e.g., Zonneveld et al., 2013). The identified epicystal Goniodomids, which in the modern ocean are typical of lagoonal, hypersaline settings (Zonneveld et al., 2013) are notably *Homotryblium* spp. and have been linked to strong stratification (and even harmful algal blooms in some cases) in the paleodomain (Brinkhuis, 1994; Pross and Schmiedl, 2002; Reichart et al., 2004; Cramwinckel et al., 2019). In effect, a major signal in the dinocysts assemblages is the sporadic dominance of *Homotryblium* spp., reaching above 90% of the identified component of the assemblages. In the middle part of the

core, we record a few more numerous and/or prolonged occurrences of representatives of *Apectodinium*, *Areoligera*, Protoperidiniods and a single occurrence of a representative of *Senegalinum*.

4. Discussion

4.1 Carbon isotope magnitude

The magnitude of the V-related CIE differs strongly between the bulk organic and carbonate records at Site 959 ($\Delta^{13}C_{carb}$ = 3.4 ‰, $\Delta^{13}C_{TOC}$ = 0.7 ‰). Importantly, the $\delta^{13}C_{carb}$ excursion is much larger than what is expected from the global exogenic signal, approximately ~0.6 ‰ (Fig. 4) (Sexton et al., 2011; Lauretano et al., 2016). We surmise that in the sedimentary environment of early Eocene Site 959, with relatively low biogenic $CaCO_3$ accumulation, authigenic carbonates, which are typically ^{13}C-depleted due to local organic carbon respiration (e.g., Botz et al., 1988), comprise a significant component of the bulk carbonate, similar to observations during earlier Eocene CIEs I1–L2 at Site 959 (Fokkema et al., 2023) and consistent with pore-water analysis (Mascle et al., 1996). Low $\delta^{13}C_{carb}$ values typically correspond with low $CaCO_3$wt% in lower Eocene deep ocean records (Zachos et al., 2010; Kirtland Turner et al., 2014). Consequently, this would exaggerate both background variability and the magnitude of the CIE in our record due to an increased fraction of authigenic carbonate in intervals with relatively low biogenic $CaCO_3$wt%.

4.2 Paleoenvironment and water column structure

4.2.1 Background climate state and oceanography

An open marine early Eocene depositional setting at Site 959 is reflected by the very low BIT index values (<0.01; Supplementary Fig. S2), generally low numbers of terrestrial palynomorphs (mean = 4.8 %) (Fig. 3a), and bulk $\delta^{13}C_{TOC}$ values around -27 ‰, indicative of marine particulate organic carbon for this time interval (Hayes et al., 1999; Sluijs and Dickens, 2012). Also the dinocyst assemblages are consistent with an open ocean setting with the continuous abundances of *Spiniferites* and particularly a few representatives of the open-ocean genus *Impagidinium* (Frieling and Sluijs, 2018). In contrast with these records, multiple samples are dominated by epicystal Goniodomid-cysts, specifically *Homotryblium* spp. (>75% of the relative dinocyst assemblage), traditionally interpreted to reflect lagoonal, hypersaline conditions (Brinkhuis, 1994; Pross and Schmiedl, 2002). However, dominances of such types of dinocysts have also been recorded under unequivocal open-ocean conditions, including the Eocene Site 959 (Frieling et al., 2018; Cramwinckel et al., 2019; Fokkema et al., 2023), attributed to so-called ‘hyper-stratified conditions’–potentially under high temperature (Cramwinckel et al., 2019), analogous to records from the ‘hyperstratified’ episodes during the Pleistocene of the Arabian Sea (cf. Reichart et al., 2004), which enables a lifecycle without a sea floor interface. It is possible that the acmes we record here indeed reflect actual ancient dinoflagellate blooms, which is common in modern representatives of this group, e.g., *Pyrodinium bahamense* and its cyst *Polysphaeridium zoharii* (Usup et al., 2012). In the paleo-domain, such a bloom-forming strategy of this group is supported by very high $\delta^{13}C$ values of *Eocladopyxis peniculata* cysts in an acme during the PETM on the New Jersey shelf (Sluijs et al., 2018). Hence, given the absence of evidence for large-scale transport of organic matter off the shelf, we suggest that the *Homotryblium* acmes/blooms at Site 959 occurred under warm and strongly stratified oceanic

conditions. We postulate that the few intervals of relatively high contribution of terrestrial palynomorphs (Fig. 3c) (partly) result from preservation bias, as terrestrial palynomorphs are more resistant to degradation than dinocysts.

The consistent presence of *Protoperidinium* cysts, derived from heterotrophic dinoflagellates, implies sufficient food supply (Zonneveld et al., 2013). Moreover, sufficient organic material must have reached the ocean floor to sustain the relatively high TOCwt% and abundance of benthic foraminifera linings. The required high primary productivity presumably originated from regional wind-driven upwelling, inferred to occur at least since the middle Eocene based on organic geochemical data and palynological data (Wagner, 2002; Cramwinckel et al., 2018). Importantly, this productive setting around 49.7 Ma contrasts the records from ~54–52 Ma, where rich dinocyst assemblages lack Protoperidinioids (Fokkema et al., 2023), suggesting that Eocene upwelling at Site 959 did not intensify until the end of the early Eocene (i.e., ~52–50 Ma). Neogene upwelling conditions at this site have previously been linked to the annual migration of the Atlantic Intertropical Convergence Zone (ITCZ) and the resulting West-African monsoonal response (Vallé et al., 2017; Wubben et al., in press). Simulations suggest that West African monsoons should already have established during the Cretaceous and early Paleogene, and were relatively strong in this time interval compared to the Miocene due to the narrower Atlantic basin (Acosta et al., 2022). Based on the dominant factors enhancing the strength of monsoons, e.g., geography and topography (Acosta et al., 2022), we infer that upwelling potentially started or intensified during the Eocene by progressive northward movement of the African plate, drifting Site 959 towards the equator.

4.2.2 Orbital variability

The regular alternations observed in multiple proxy records (e.g., $CaCO_3$ content, MS, Fe, TOC%, total GDGT concentration), specifically on ~50-cm scale below the CIE (759.5–757.4 mbsf), suggests an orbital influence on the local oceanographic conditions and/or monsoon strength, analogous to that recorded in the Cretaceous (Beckmann et al., 2005) and Miocene (Wubben et al., in press) at Site 959. As there is only one age-depth tiepoint in the studied core section, the responsible orbital cycle cannot be confidently identified. Although sedimentation rates of the studied section are uncertain, the long-term background sedimentation rates of 0.8–1.4 cm/kyr (Fokkema et al., 2023) imply that the persistent 50-cm variability would approximate the 41-kyr obliquity band. However, obliquity has neglectable direct influence on equatorial insolation, whereas variability in the strength of the monsoons is usually associated with Earth's ~20-kyr precession cycles, and only obliquity when remotely forced (e.g., Tuenter et al., 2003). On the other hand, dominant obliquity forcing has been observed in low latitudes (Weedon et al., 1997) and exerts influence on Neogene Mediterranean sapropel occurrences and monsoon dynamics (e.g., Lourens et al., 1996; Bosmans et al., 2015). In addition, obliquity is also possibly more pronounced under very low orbital eccentricity configurations (Westerhold et al., 2014), as also recorded in the early Miocene at Site 959 (Wubben et al., 2023). Indeed, a ~2.4-Myr orbital-eccentricity minimum just precedes the V event (Laskar et al., 2011; Lauretano et al., 2018) (Fig. 4), supporting the possibility of obliquity forcing on monsoonal strength prior to V. Nevertheless, without additional age control, there remains a possibility that the cyclic variations prior to V represent precession.

The cycles below the V event coincide with temperature variability of 0.8–1 ºC. This variability is mirrored in $\delta^{13}C_{TOC}$, with minimum TEX_{86} values coinciding with $\delta^{13}C_{TOC}$ minima,

which suggests that during enhanced upwelling of ^{13}C depleted subsurface waters, the shallow waters cooled and vice versa (Fig. 3). No clear cyclic patterns are present in the interval above V. Importantly, the absence of the W CIE, which occurred ~100 kyr after V, implies at least a doubling of sedimentation rate if the pre-event variations represent obliquity. Accordingly, a relative increase in, $CaCO_3$, Si and TOCwt% (Fig. 3a) suggest higher productivity and biogenic sediment accumulation rates compared to the lower interval, potentially facilitating the required increase if the supply of siliciclastic materials remained constant.

4.2.3 Environmental change during hyperthermal V

The peak SSTs reached during the V event of 36.1 ºC are consistent with the hyperthermals in the earlier interval of the Eocene (Fokkema et al., 2023). The magnitude of warming (ΔT = 1.1–1.9 ºC) is, however, higher than recorded during the preceding early Eocene hyperthermals at Site 959 (averaged ~0.7–1 ºC; (Fokkema et al., 2023)). Peak warmth during hyperthermal V manifests in two peaks (757.0 & 756.5) separated by a plateau. We surmise that this reflects a continuation of the pre-event orbitally forced variability in monsoon strength. Accordingly, the two temperature peaks are marked by relatively high $\delta^{13}C_{TOC}$ values, suggesting they represent periods of minimal upwelling, similar to the intervals of higher $\delta^{13}C_{TOC}$ and SST surrounding the event.

In addition to warming, the V event is characterized by increased TOCwt%, Fe, MS and a decline in the $CaCO_3$ wt% and Si in the sediment. Frieling et al. (2018) discussed multiple mechanisms that might have induced low $CaCO_3$ wt% contents in PETM records at Site 959. Ocean acidification may well have impacted carbonate preservation, but this may have been limited, due to the relatively shallow paleodepth (~1000 m) of Site 959 during the early Eocene (Frieling et al., 2018). However, similar to the PETM interpretation by Frieling et al. (2018), we infer that the low $CaCO_3$wt% during the CIE can be attributed to remineralization of organic material in the sediment and possibly also to attenuation of biogenic $CaCO_3$ formation– potentially by heat stress (Aze et al., 2014; Frieling et al., 2018).

Although — as discussed above — dinocyst preservation being poor in general, we do record a subtle dinocyst response during hyperthermal V. Notably, few occurrences of the thermophilic dinocyst taxon *Apectodinium* are recorded during the hyperthermal (Fig. 3c). Representatives of this genus are known to occur in high numbers surrounding the PETM interval at Site 959 (Frieling et al., 2018) (and globally during the PETM, e.g., Crouch et al., 2001; Denison, 2021). Presumably other factors than solely temperature allowed for the occurance of *Apectodinium* spp. to Site 959; perhaps the supply of nutrients. Another feature is abundant *Areoligera* spp. at 756.8 mbsf. This peak coincides with the highest relative abundance of dinocysts (>75%), and elevated TOCwt% (Fig. 2). Although perhaps masked by poor preservation, the epicystal Goniodomid-cysts do not seem to significantly increase during the event, conflicting with the occurrence of (thermal) hyperstratification during the peak MECO (Cramwinckel et al., 2019).

4.3 Polar amplification of climate change

Previous work has compared the warming of early Eocene hyperthermals in the tropics to that of higher latitudes to assess ice-free polar amplification of climate change, finding a relative consistent amplification factor of approximately ~2 (Frieling et al., 2017; Tierney et al., 2022; Fokkema et al., 2023). The only temperature and ecological records from the high latitudes that

cover internal climate variability in the EECO (i.e. IODP Site 1356, Wilkes Land) are still not fully resolved on eccentricity timescales (Pross et al., 2012; Bijl et al., 2013). Therefore, to assess potential extratropical amplification of warming during hyperthermal V, we compare the warming at Site 959 with that in the deep ocean benthic foraminiferal $\delta^{18}O$-based bottom water temperature (BWT) records, following the approach of Cramwinckel et al. (2018) and Fokkema et al. (2023). Importantly, the $\delta^{18}O$-based BWTs match the pollen-derived coldest month temperatures at Wilkes Land (Pross et al., 2012), in line with the notion that early Eocene bottom water formation occurred dominantly in the Southern Ocean close to the Antarctic margin (Hollis et al., 2012; Zhang et al., 2022). In the deep ocean, hyperthermal V was marked by a warming of ~1.5 ºC (Lauretano et al., 2018) (Fig. 4). This implies a near-absent amplification of warming between the tropics and the polar region of deep-water formation (0.8–1.4), which mismatches the polar amplification recorded during multiple early EECO hyperthermals (1.7–2.2) (Fokkema et al., 2023) and during the PETM ~1.6–2.7 (Frieling et al., 2017; Tierney et al., 2022). We surmise that the upwelling at Site 959 during this interval led to reduced polar amplification estimates, possibly due to a decrease in upwelling intensity during the V event, amplifying surface warming at Site 959.

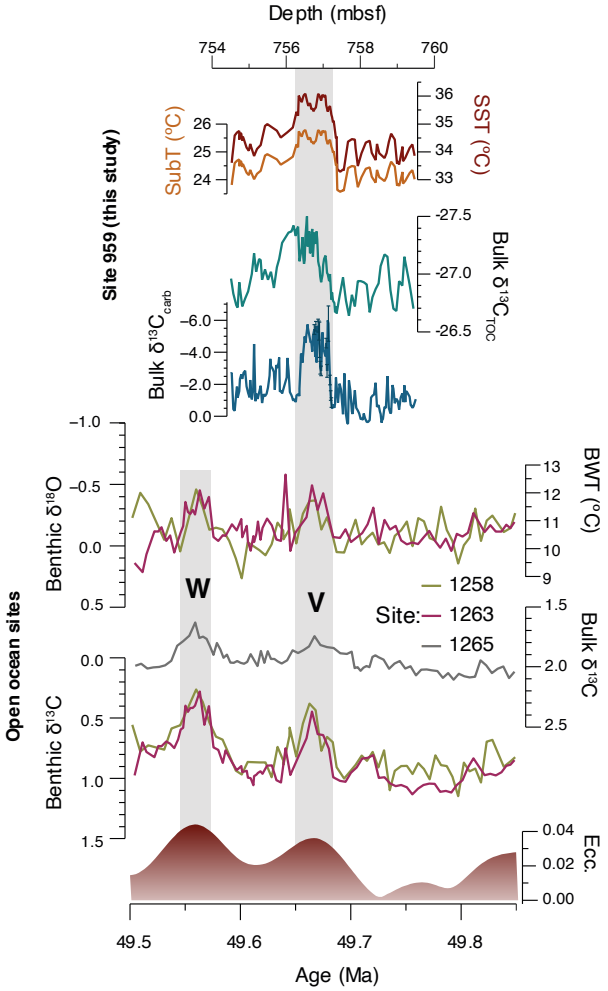

Figure 4. Representation of the V event at Site 959 and other Atlantic Ocean sites. Top: Site 959 data (against depth) with TEX_{86}-based SST and SubT, $\delta^{13}C_{TOC}$ and $\delta^{13}C_{carb}$. Bottom: benthic $\delta^{18}O$ from Site 1258 (Sexton et al., 2011) and Site 1263 (Lauretano et al., 2016, 2018) with $\delta^{18}O$-based bottom water temperatures on the right (following (Kim and O'Neil, 1997), modified by (Bemis et al., 1998) and seawater $\delta^{18}O$ of -1‰ VPDB). Bulk $\delta^{13}C$ from Site 1265 (Westerhold et al., 2017), benthic $\delta^{13}C$ of Site 1258 and 1263 and orbital eccentricity (Laskar et al., 2011). Grey bands mark globally recognized CIEs V and W.

4.4 Prolonged organic carbon isotope excursion

The recovery of the CIEs in the $\delta^{13}C_{TOC}$ and $\delta^{13}C_{carb}$ are significantly offset; $\delta^{13}C_{TOC}$ lags $\delta^{13}C_{carb}$ by 55 cm, which represents ~40–70 kyr, following long-term background sedimentation rates of 0.8–1.4 cm/kyr (calculated between Top *Tribarchaitus orthostylus* (Core 36R) and Top *Discoaster lodoensis* (Core 39R–Core 38R); Fig. 2). This is inconsistent with the premise that carbon utilized in photosynthesis and calcification are both fixed from the same dissolved inorganic carbon (DIC) pool. It suggests that an organic matter component with low $\delta^{13}C$ values contributes to sedimentary $\delta^{13}C_{TOC}$ values in the direct aftermath of the CIE. Potentially, the longer tail in the $\delta^{13}C_{TOC}$ record represents terrestrial organic carbon produced during the CIE, transported to the marine realm after the event. However, this is inconsistent with the relatively short (~5 kyr) time between the production of terrestrial organic matter and its transport to the ocean (Cole and Caraco, 2001) and the consistently low relative amounts of terrestrial organic matter in our materials.

In the modern ocean, the oldest (most ^{14}C-depleted) phase of carbon resides as (refractory) dissolved organic carbon (DOC_{ref}) in the Pacific Ocean at 2 km water depth, with an estimated age of 12 kyrs (Follett et al., 2014). Potentially, the long bulk $\delta^{13}C_{TOC}$ tail thus reflects contributions from this older DOC_{ref} pool in the aftermath of V. This chemically inert phase of DOC is likely generated by the microbial carbon pump (Jiao et al., 2010). The bioavailability of DOC_{ref} increases by upwelling (Fang et al., 2020), which allows for a biotic conversion of ^{13}C-depleted DOC_{ref} to ^{13}C-depleted POC (Shen and Benner, 2018). Specifically, DOC_{ref} is suggested to physically disintegrate by radiation at the surface ocean and biologically degrade by the addition of more readily degradable organic matter (Shen and Benner, 2018; Fang et al., 2020). Furthermore, based on the presence of sponge spicules in younger intervals at Site 959 (Mascle et al., 1996), while they would not be well preserved in the Eocene porcellanites, this site might facilitate the DOC to POC conversion by benthic filter feeding sponges. We surmise that Site 959 holds the potential to transform $\delta^{13}C$ depleted DOC_{ref} to POC, either at the surface and/or the deep ocean, which will eventually leave an imprint in the sediment record as a prolonged $\delta^{13}C_{TOC}$ tail.

Conclusions

Tropical warming and biotic change accompanied a significant CIE during the end of the EECO in the tropical Atlantic at Site 959. By previously published biostratigraphic constraints and new carbon isotope stratigraphy the CIE is identified as the "V" event at 49.7 Ma. TEX_{86} paleothermometry indicates a temperature increase of 1.1–1.9 °C relative to pre-event values, confirming that this event represents a transient global warming event, or hyperthermal. Peak temperatures during V (SSTs of ~36.1 °C) match that of earlier hyperthermals during the EECO.

Interestingly, the recovery of the CIE in $\delta^{13}C_{TOC}$ is delayed relative to that in $\delta^{13}C_{carb}$. We postulate that upwelling of old and deep (^{13}C-depleted) DOC_{ref} contributed to the long bulk $\delta^{13}C_{TOC}$ tail.

The recorded background paleoceanography during this time differs from earlier Eocene records from the same site: wind-driven upwelling facilitated a more productive depositional setting reflected in relatively organic rich sediments and presence of heterotrophic dinoflagellate cyst remains. Variations in upwelling intensity, presumably orbitally driven by monsoons, are reflected in multiple proxy indicators: notably affecting carbon isotopes and temperatures in the (shallow sub-) surface ocean. In strong contrast to the recorded upwelling is the sporadic dinocyst dominance by hyper-stratification-related genera, which seems a common feature in Eocene Site 959 records (Frieling et al., 2018; Cramwinckel et al., 2019; Fokkema et al., 2023).

Acknowledgements

This project used samples retrieved and curated by the IODP and predecessors. We thank Antoinette van den Dikkenberg, Natasja Welters, Giovanni Dammers., Desmond Eefting, Maxim Krasnoperov and Arnold van Dijk for their assistance in the lab and technical support. This research was funded by European Research Council Grant 771497 awarded to A. Sluijs under the H2020 program, by the Deutsche Forschungsgemeinschaft (DFG, German Research Foundation) to U.R. and T.W. (project nos. 28504316 and 320221997) and under Germany´s Excellence Strategy–EXC-2077–390741603. Extended Partnership funded by European Union Next-GenerationEU (National Recovery and Resilience Plan–NRRP, Mission 4, Component 2, Investment 1.3–D.D. 1243 2/8/2022, PE0000005.

Competing interests

One of the co-authors is a member of the editorial board of Paleoceanography and Paleoclimatology.

Open Research

All new data presented in this work will be made publicly available on Zenodo upon publication.

References

Acosta, R. P., Ladant, J., Zhu, J., & Poulsen, C. J. (2022). Evolution of the Atlantic Intertropical Convergence Zone, and the South American and African Monsoons Over the Past 95-Myr and Their Impact on the Tropical Rainforests. Paleoceanography and Paleoclimatology, 37(7), e2021PA004383. https://doi.org/10.1029/2021PA004383

Agnini, C., Muttoni, G., Kent, D. V., & Rio, D. (2006). Eocene biostratigraphy and magnetic stratigraphy from Possagno, Italy: The calcareous nannofossil response to climate variability. Earth and Planetary Science Letters, 241(3–4), 815–830. https://doi.org/10.1016/j.epsl.2005.11.005

Agnini, C., Macrì, P., Backman, J., Brinkhuis, H., Fornaciari, E., Giusberti, L., et al. (2009). An early Eocene carbon cycle perturbation at ~52.5 Ma in the Southern Alps: Chronology and biotic response. Paleoceanography, 24(2), PA2209. https://doi.org/10.1029/2008PA001649

600 Agnini, C., Fornaciari, E., Raffi, I., Catanzariti, R., Pälike, H., Backman, J., & Rio, D. (2014).
601 Biozonation and biochronology of Paleogene calcareous nannofossils from low and middle
602 latitudes. Newsletters on Stratigraphy, 47(2), 131–181. https://doi.org/10.1127/0078-
603 0421/2014/0042

604 Anagnostou, E., John, E. H., Babila, T. L., Sexton, P. F., Ridgwell, A., Lunt, D. J., et al. (2020).
605 Proxy evidence for state-dependence of climate sensitivity in the Eocene greenhouse.
606 Nature Communications, 11(1), 4436. https://doi.org/10.1038/s41467-020-17887-x

607 Aze, T., Pearson, P. N., Dickson, A. J., Badger, M. P. S., Bown, P. R., Pancost, R. D., et al. (2014).
608 Extreme warming of tropical waters during the Paleocene–Eocene Thermal Maximum.
609 Geology, 42(9), 739–742. https://doi.org/10.1130/G35637.1

610 Backman, J. (1986). Late Paleocene to middle Eocene calcareous nannofossil biochronology from
611 the Shatsky Rise, Walvis Ridge and Italy. Palaeogeography, Palaeoclimatology,
612 Palaeoecology, 57(1), 43–59. https://doi.org/10.1016/0031-0182(86)90005-2

613 Beckmann, B., Flögel, S., Hofmann, P., Schulz, M., & Wagner, T. (2005). Orbital forcing of
614 Cretaceous river discharge in tropical Africa and ocean response. Nature, 437(7056), 241–
615 244. https://doi.org/10.1038/nature03976

616 Bemis, B. E., Spero, H. J., Bijma, J., & Lea, D. W. (1998). Reevaluation of the oxygen isotopic
617 composition of planktonic foraminifera: Experimental results and revised
618 paleotemperature equations. Paleoceanography, 13(2), 150–160.
619 https://doi.org/10.1029/98PA00070

620 Berndt, C., Planke, S., Alvarez Zarikian, C. A., Frieling, J., Jones, M. T., Millett, J. M., et al. (2023).
621 Shallow-water hydrothermal venting linked to the Palaeocene–Eocene Thermal Maximum.
622 Nature Geoscience, 16(9), 803–809. https://doi.org/10.1038/s41561-023-01246-8

623 Bijl, P. K., Schouten, S., Sluijs, A., Reichart, G.-J., Zachos, J. C., & Brinkhuis, H. (2009). Early
624 Palaeogene temperature evolution of the southwest Pacific Ocean. Nature, 461(7265),
625 776–779. https://doi.org/10.1038/nature08399

626 Bijl, P. K., Bendle, J. A. P., Bohaty, S. M., Pross, J., Schouten, S., Tauxe, L., et al. (2013). Eocene
627 cooling linked to early flow across the Tasmanian Gateway. Proceedings of the National
628 Academy of Sciences, 110(24), 9645–9650. https://doi.org/10.1073/pnas.1220872110

629 Bijl, P. K., Frieling, J., Cramwinckel, M. J., Boschman, C., Sluijs, A., & Peterse, F. (2021).
630 Maastrichtian–Rupelian paleoclimates in the southwest Pacific – a critical re-evaluation of
631 biomarker paleothermometry and dinoflagellate cyst paleoecology at Ocean Drilling
632 Program Site 1172. Climate of the Past, 17(6), 2393–2425. https://doi.org/10.5194/cp-17-
633 2393-2021

634 Bosmans, J. H. C., Drijfhout, S. S., Tuenter, E., Hilgen, F. J., & Lourens, L. J. (2015). Response
635 of the North African summer monsoon to precession and obliquity forcings in the EC-Earth
636 GCM. Climate Dynamics, 44(1–2), 279–297. https://doi.org/10.1007/s00382-014-2260-z

637 Botz, R., Faber, E., Whiticar, M. J., & Brooks, J. M. (1988). Authigenic carbonates in sediments
638 from the Gulf of Mexico. Earth and Planetary Science Letters, 88(3–4), 263–272.
639 https://doi.org/10.1016/0012-821X(88)90083-0

640 Brinkhuis, H. (1994). Late Eocene to Early Oligocene dinoflagellate cysts from the Priabonian
641 type-area (Northeast Italy): biostratigraphy and paleoenvironmental interpretation.
642 Palaeogeography, Palaeoclimatology, Palaeoecology, 107(1–2), 121–163.
643 https://doi.org/10.1016/0031-0182(94)90168-6

644 Cappelli, C., Bown, P. R., Westerhold, T., Bohaty, S. M., Riu, M., Lobba, V., et al. (2019). The
645 Early to Middle Eocene Transition: An Integrated Calcareous Nannofossil and Stable
646 Isotope Record From the Northwest Atlantic Ocean (Integrated Ocean Drilling Program
647 Site U1410). Paleoceanography and Paleoclimatology, 34(12), 1913–1930.
648 https://doi.org/10.1029/2019PA003686

649 Cole, J. J., & Caraco, N. F. (2001). Carbon in catchments: connecting terrestrial carbon losses with
650 aquatic metabolism. Marine and Freshwater Research, 52(1), 101.
651 https://doi.org/10.1071/MF00084

652 Cramer, B. S., Wright, J. D., Kent, D. V., & Aubry, M.-P. (2003). Orbital climate forcing of D13C
653 excursions in the late Paleocene—early Eocene (chrons C24n–C25n). Paleoceanography,
654 18, 1097. https://doi.org/10.1029/2003PA000909

655 Cramwinckel, M. J., Huber, M., Kocken, I. J., Agnini, C., Bijl, P. K., Bohaty, S. M., et al. (2018).
656 Synchronous tropical and polar temperature evolution in the Eocene. Nature, 559(7714),
657 382–386. https://doi.org/10.1038/s41586-018-0272-2

658 Cramwinckel, M. J., van der Ploeg, R., Bijl, P. K., Peterse, F., Bohaty, S. M., Röhl, U., et al. (2019).
659 Harmful algae and export production collapse in the equatorial Atlantic during the zenith
660 of Middle Eocene Climatic Optimum warmth. Geology, 47(3), 247–250.
661 https://doi.org/10.1130/G45614.1

662 Crouch, E. M., Heilmann-Clausen, C., Brinkhuis, H., Morgans, H. E. G., Rogers, K. M., Egger,
663 H., & Schmitz, B. (2001). Global dinoflagellate event associated with the late Paleocene
664 thermal maximum. Geology, 29(4), 315. https://doi.org/10.1130/0091-
665 7613(2001)029<0315:GDEAWT>2.0.CO;2

666 DeConto, R. M., Galeotti, S., Pagani, M., Tracy, D., Schaefer, K., Zhang, T., et al. (2012). Past
667 extreme warming events linked to massive carbon release from thawing permafrost.
668 Nature, 484(7392), 87–91. https://doi.org/10.1038/nature10929

669 Denison, C. N. (2021). Stratigraphic and sedimentological aspects of the worldwide distribution
670 of Apectodinium in Paleocene/Eocene Thermal Maximum deposits. In F. Marret, J.
671 O'Keefe, P. Osterloff, M. Pound, & L. Shumilovskikh (Eds.), Applications of Non-Pollen
672 Palynomorphs: from Palaeoenvironmental Reconstructions to Biostratigraphy (p. 0).
673 Geological Society of London. https://doi.org/10.1144/SP511-2020-46

674 Dickens, G. R., O'Neil, J. R., Rea, D. K., & Owen, R. M. (1995). Dissociation of oceanic methane
675 hydrate as a cause of the carbon isotope excursion at the end of the Paleocene.
676 Paleoceanography, 10(6), 965–971. https://doi.org/10.1029/95PA02087

677 Dickens, G. R., Castillo, M. M., & Walker, J. C. G. (1997). A blast of gas in the latest Paleocene:
678 Simulating first-order effects of massive dissociation of oceanic methane hydrate. Geology,
679 25(3), 259. https://doi.org/10.1130/0091-7613(1997)025<0259:ABOGIT>2.3.CO;2

680 Dunkley Jones, T., Lunt, D. J., Schmidt, D. N., Ridgwell, A., Sluijs, A., Valdes, P. J., & Maslin, M.
681 (2013). Climate model and proxy data constraints on ocean warming across the Paleocene–
682 Eocene Thermal Maximum. Earth-Science Reviews, 125, 123–145.
683 https://doi.org/10.1016/j.earscirev.2013.07.004

684 Fang, L., Lee, S., Lee, S.-A., Hahm, D., Kim, G., Druffel, E. R. M., & Hwang, J. (2020). Removal
685 of Refractory Dissolved Organic Carbon in the Amundsen Sea, Antarctica. Scientific
686 Reports, 10(1), 1213. https://doi.org/10.1038/s41598-020-57870-6

687 Fokkema, C. D., Buijs, S., Bialik, O. M., Meilijson, A., Waldmann, N. D., Makovsky, Y., et al.
688 (2022). Late Paleocene to middle Eocene carbon isotope stratigraphy of the Northern
689 Negev, Southern Israel: potential for paleoclimate reconstructions. Newsletters on
690 Stratigraphy, 55(3), 361–384. https://doi.org/10.1127/nos/2022/0684

691 Fokkema, C. D., Agterhuis, T., Gerritsma, D., De Goeij, M., Liu, X., De Regt, P., et al. (2023).
692 Polar amplification of orbital-scale climate variability in the early Eocene greenhouse
693 world (Preprint). Climate of the Past Discussions. https://doi.org/10.5194/cp-2023-70

694 Follett, C. L., Repeta, D. J., Rothman, D. H., Xu, L., & Santinelli, C. (2014). Hidden cycle of
695 dissolved organic carbon in the deep ocean. Proceedings of the National Academy of
696 Sciences, 111(47), 16706–16711. https://doi.org/10.1073/pnas.1407445111

697 Frieling, J., Svensen, H. H., Planke, S., Cramwinckel, M. J., Selnes, H., & Sluijs, A. (2016).
698 Thermogenic methane release as a cause for the long duration of the PETM. Proceedings
699 of the National Academy of Sciences, 113(43), 12059–12064.
700 https://doi.org/10.1073/pnas.1603348113

701 Frieling, J., Reichart, G. J., Middelburg, J. J., Rohl, U., Westerhold, T., Bohaty, S. M., & Sluijs, A.
702 (2018). Tropical Atlantic climate and ecosystem regime shifts during the Paleocene–
703 Eocene Thermal Maximum. Climate of the Past, 14(1), 39–55. https://doi.org/10.5194/cp-
704 14-39-2018

705 Frieling, J., Peterse, F., Lunt, D. J., Bohaty, S. M., Sinninghe Damsté, J. S., Reichart, G.-J., &
706 Sluijs, A. (2019). Widespread Warming Before and Elevated Barium Burial During the
707 Paleocene-Eocene Thermal Maximum: Evidence for Methane Hydrate Release?
708 Paleoceanography and Paleoclimatology, 34(4), 546–566.
709 https://doi.org/10.1029/2018PA003425

710 Frieling, Joost, & Sluijs, A. (2018). Towards quantitative environmental reconstructions from
711 ancient non-analogue microfossil assemblages: Ecological preferences of Paleocene –

712 Eocene dinoflagellates. Earth-Science Reviews, 185, 956–973.
713 https://doi.org/10.1016/j.earscirev.2018.08.014

714 Frieling, Joost, Gebhardt, H., Huber, M., Adekeye, O. A., Akande, S. O., Reichart, G.-J., et al.
715 (2017). Extreme warmth and heat-stressed plankton in the tropics during the Paleocene-
716 Eocene Thermal Maximum. Science Advances, 3(3), e1600891.
717 https://doi.org/10.1126/sciadv.1600891

718 Galeotti, S., Krishnan, S., Pagani, M., Lanci, L., Gaudio, A., Zachos, J. C., et al. (2010). Orbital
719 chronology of Early Eocene hyperthermals from the Contessa Road section, central Italy.
720 Earth and Planetary Science Letters, 290(1–2), 192–200.
721 https://doi.org/10.1016/j.epsl.2009.12.021

722 Gaskell, D. E., Huber, M., O'Brien, C. L., Inglis, G. N., Acosta, R. P., Poulsen, C. J., & Hull, P. M.
723 (2022). The latitudinal temperature gradient and its climate dependence as inferred from
724 foraminiferal δ 18 O over the past 95 million years. Proceedings of the National Academy
725 of Sciences, 119(11), e2111332119. https://doi.org/10.1073/pnas.2111332119

726 Gibbs, S. J., Bown, P. R., Murphy, B. H., Sluijs, A., Edgar, K. M., Pälike, H., et al. (2012). Scaled
727 biotic disruption during early Eocene global warming events. Biogeosciences, 9(11), 4679–
728 4688. https://doi.org/10.5194/bg-9-4679-2012

729 Hayes, J. M., Strauss, H., & Kaufman, A. J. (1999). The abundance of 13C in marine organic
730 matter and isotopic fractionation in the global biogeochemical cycle of carbon during the
731 past 800 Ma. Chemical Geology, 161(1–3), 103–125. https://doi.org/10.1016/S0009-
732 2541(99)00083-2

733 van Hinsbergen, D. J. J., de Groot, L. V., van Schaik, S. J., Spakman, W., Bijl, P. K., Sluijs, A., et
734 al. (2015). A Paleolatitude Calculator for Paleoclimate Studies. PLOS ONE, 10(6),
735 e0126946. https://doi.org/10.1371/journal.pone.0126946

736 Ho, S. L., & Laepple, T. (2016). Flat meridional temperature gradient in the early Eocene in the
737 subsurface rather than surface ocean. Nature Geoscience, 9(8), 606–610.
738 https://doi.org/10.1038/ngeo2763

739 Hollis, C. J., Taylor, K. W. R., Handley, L., Pancost, R. D., Huber, M., Creech, J. B., et al. (2012).
740 Early Paleogene temperature history of the Southwest Pacific Ocean: Reconciling proxies
741 and models. Earth and Planetary Science Letters, 349–350, 53–66.
742 https://doi.org/10.1016/j.epsl.2012.06.024

743 Hopmans, E. C., Weijers, J. W. H., Schefuß, E., Herfort, L., Sinninghe Damsté, J. S., & Schouten,
744 S. (2004). A novel proxy for terrestrial organic matter in sediments based on branched and
745 isoprenoid tetraether lipids. Earth and Planetary Science Letters, 224(1–2), 107–116.
746 https://doi.org/10.1016/j.epsl.2004.05.012

747 Hopmans, E. C., Schouten, S., & Sinninghe Damsté, J. S. (2016). The effect of improved
748 chromatography on GDGT-based palaeoproxies. Organic Geochemistry, 93, 1–6.
749 https://doi.org/10.1016/j.orggeochem.2015.12.006

Hupp, B. N., Kelly, D. C., & Williams, J. W. (2022). Isotopic filtering reveals high sensitivity of planktic calcifiers to Paleocene–Eocene thermal maximum warming and acidification. Proceedings of the National Academy of Sciences, 119(9), e2115561119. https://doi.org/10.1073/pnas.2115561119

Hurley, S. J., Lipp, J. S., Close, H. G., Hinrichs, K.-U., & Pearson, A. (2018). Distribution and export of isoprenoid tetraether lipids in suspended particulate matter from the water column of the Western Atlantic Ocean. Organic Geochemistry, 116, 90–102. https://doi.org/10.1016/j.orggeochem.2017.11.010

Inglis, G. N., Bragg, F., Burls, N. J., Cramwinckel, M. J., Evans, D., Foster, G. L., et al. (2020). Global mean surface temperature and climate sensitivity of the early Eocene Climatic Optimum (EECO), Paleocene–Eocene Thermal Maximum (PETM), and latest Paleocene. Climate of the Past, 16(5), 1953–1968. https://doi.org/10.5194/cp-16-1953-2020

Jiao, N., Herndl, G. J., Hansell, D. A., Benner, R., Kattner, G., Wilhelm, S. W., et al. (2010). Microbial production of recalcitrant dissolved organic matter: long-term carbon storage in the global ocean. Nature Reviews Microbiology, 8(8), 593–599. https://doi.org/10.1038/nrmicro2386

Kennett, J. P., & Stott, L. D. (1991). Abrupt deep-sea warming, palaeoceanographic changes and benthic extinctions at the end of the Palaeocene. Nature, 353(6341), 225–229. https://doi.org/10.1038/353225a0

Kim, J.-H., van der Meer, J., Schouten, S., Helmke, P., Willmott, V., Sangiorgi, F., et al. (2010). New indices and calibrations derived from the distribution of crenarchaeal isoprenoid tetraether lipids: Implications for past sea surface temperature reconstructions. Geochimica et Cosmochimica Acta, 74(16), 4639–4654. https://doi.org/10.1016/j.gca.2010.05.027

Kim, S.-T., & O'Neil, J. R. (1997). Equilibrium and nonequilibrium oxygen isotope effects in synthetic carbonates. Geochimica et Cosmochimica Acta, 61(16), 3461–3475. https://doi.org/10.1016/S0016-7037(97)00169-5

Kirtland Turner, S., Sexton, P. F., Charles, C. D., & Norris, R. D. (2014). Persistence of carbon release events through the peak of early Eocene global warmth. Nature Geoscience, 7(10), 748–751. https://doi.org/10.1038/ngeo2240

Kocken, I. J. (2022). colourlog: generate plots of colourlogs from core photographs. https://doi.org/10.5281/zenodo.7277860

Kurtz, A. C., Kump, L. R., Arthur, M. A., Zachos, J. C., & Paytan, A. (2003). Early Cenozoic decoupling of the global carbon and sulfur cycles. Paleoceanography, 18(4), 1090. https://doi.org/10.1029/2003PA000908

Laskar, J., Fienga, A., Gastineau, M., & Manche, H. (2011). La2010: a new orbital solution for the long-term motion of the Earth. Astronomy & Astrophysics, 532, A89. https://doi.org/10.1051/0004-6361/201116836

787 Lauretano, V., Hilgen, F. J., Zachos, J. C., & Lourens, L. J. (2016). Astronomically tuned age model
788 for the early Eocene carbon isotope events: A new high-resolution δ13 Cbenthic record of
789 ODP Site 1263 between ~ 49 and ~ 54 Ma. Newsletters on Stratigraphy, 49(2), 383–400.
790 https://doi.org/10.1127/nos/2016/0077

791 Lauretano, Vittoria, Zachos, J. C., & Lourens, L. J. (2018). Orbitally Paced Carbon and Deep-Sea
792 Temperature Changes at the Peak of the Early Eocene Climatic Optimum.
793 Paleoceanography and Paleoclimatology, 33(10), 1050–1065.
794 https://doi.org/10.1029/2018PA003422

795 Laurin, J., Meyers, S. R., Galeotti, S., & Lanci, L. (2016). Frequency modulation reveals the
796 phasing of orbital eccentricity during Cretaceous Oceanic Anoxic Event II and the Eocene
797 hyperthermals. Earth and Planetary Science Letters, 442, 143–156.
798 https://doi.org/10.1016/j.epsl.2016.02.047

799 Littler, K., Röhl, U., Westerhold, T., & Zachos, J. C. (2014). A high-resolution benthic stable-
800 isotope record for the South Atlantic: Implications for orbital-scale changes in Late
801 Paleocene–Early Eocene climate and carbon cycling. Earth and Planetary Science Letters,
802 401, 18–30. https://doi.org/10.1016/j.epsl.2014.05.054

803 Lourens, L. J., Antonarakou, A., Hilgen, F. J., Van Hoof, A. A. M., Vergnaud-Grazzini, C., &
804 Zachariasse, W. J. (1996). Evaluation of the Plio-Pleistocene astronomical timescale.
805 Paleoceanography, 11(4), 391–413. https://doi.org/10.1029/96PA01125

806 Lourens, Lucas J., Sluijs, A., Kroon, D., Zachos, J. C., Thomas, E., Röhl, U., et al. (2005).
807 Astronomical pacing of late Palaeocene to early Eocene global warming events. Nature,
808 435(7045), 1083–1087. https://doi.org/10.1038/nature03814

809 Mascle, J., Lohmann, G. P., Clift, P. D., & Shipboard Scientific Party (Eds.). (1996). Proceedings
810 of the Ocean Drilling Program, 159 Initial Reports (Vol. 159). College Station, TX, USA:
811 Ocean Drilling Program. https://doi.org/10.2973/odp.proc.ir.159.1996

812 Massana, R., DeLong, E. F., & Pedrós-Alió, C. (2000). A Few Cosmopolitan Phylotypes Dominate
813 Planktonic Archaeal Assemblages in Widely Different Oceanic Provinces. Applied and
814 Environmental Microbiology, 66(5), 1777–1787. https://doi.org/10.1128/AEM.66.5.1777-
815 1787.2000

816 McInerney, F. A., & Wing, S. L. (2011). The Paleocene-Eocene Thermal Maximum: A Perturbation
817 of Carbon Cycle, Climate, and Biosphere with Implications for the Future. Annual Review
818 of Earth and Planetary Sciences, 39(1), 489–516. https://doi.org/10.1146/annurev-earth-
819 040610-133431

820 Piedrahita, V. A., Galeotti, S., Zhao, X., Roberts, A. P., Rohling, E. J., Heslop, D., et al. (2022).
821 Orbital phasing of the Paleocene-Eocene Thermal Maximum. Earth and Planetary Science
822 Letters, 598, 117839. https://doi.org/10.1016/j.epsl.2022.117839

Pross, J., & Brinkhuis, H. (2005). Organic-walled dinoflagellate cysts as paleoenvironmental indicators in the Paleogene; a synopsis of concepts. Paläontologische Zeitschrift, 79(1), 53–59. https://doi.org/10.1007/BF03021753

Pross, J., & Schmiedl, G. (2002). Early Oligocene dinoflagellate cysts from the Upper Rhine Graben (SW Germany): paleoenvironmental and paleoclimatic implications. Marine Micropaleontology, 45, 1–24.

Pross, J., Contreras, L., Bijl, P. K., Greenwood, D. R., Bohaty, S. M., Schouten, S., et al. (2012). Persistent near-tropical warmth on the Antarctic continent during the early Eocene epoch. Nature, 488(7409), 73–77. https://doi.org/10.1038/nature11300

Rattanasriampaipong, R., Zhang, Y. G., Pearson, A., Hedlund, B. P., & Zhang, S. (2022). Archaeal lipids trace ecology and evolution of marine ammonia-oxidizing archaea. Proceedings of the National Academy of Sciences, 119(31), e2123193119. https://doi.org/10.1073/pnas.2123193119

Reichart, G.-J., Brinkhuis, H., Huiskamp, F., & Zachariasse, W. J. (2004). Hyperstratification following glacial overturning events in the northern Arabian Sea. Paleoceanography, 19(2). https://doi.org/10.1029/2003PA000900

Rush, W. D., Self-Trail, J., Zhang, Y., Sluijs, A., Brinkhuis, H., Zachos, J., et al. (2023). Assessing environmental change associated with early Eocene hyperthermals in the Atlantic Coastal Plain, USA. Climate of the Past, 19, 1677–1698. https://doi.org/10.5194/cp-19-1677-2023

Schrag, D. P., DePaolo, D. J., & Richter, F. M. (1995). Reconstructing past sea surface temperatures: Correcting for diagenesis of bulk marine carbonate. Geochimica et Cosmochimica Acta, 59(11), 2265–2278. https://doi.org/10.1016/0016-7037(95)00105-9

Setty, S., Cramwinckel, M. J., Van Nes, E. H., Van De Leemput, I. A., Dijkstra, H. A., Lourens, L. J., et al. (2023). Loss of Earth system resilience during early Eocene transient global warming events. Science Advances, 9(14), eade5466. https://doi.org/10.1126/sciadv.ade5466

Sexton, P. F., Norris, R. D., Wilson, P. A., Pälike, H., Westerhold, T., Röhl, U., et al. (2011). Eocene global warming events driven by ventilation of oceanic dissolved organic carbon. Nature, 471(7338), 349–352. https://doi.org/10.1038/nature09826

Shackleton, N. J. (1986). Paleogene stable isotope events. Palaeogeography, Palaeoclimatology, Palaeoecology, 57(1), 91–102. https://doi.org/10.1016/0031-0182(86)90008-8

Shen, Y., & Benner, R. (2018). Mixing it up in the ocean carbon cycle and the removal of refractory dissolved organic carbon. Scientific Reports, 8(1), 2542. https://doi.org/10.1038/s41598-018-20857-5

Sluijs, A., & Brinkhuis, H. (2009). A dynamic climate and ecosystem state during the Paleocene-Eocene Thermal Maximum: inferences from dinoflagellate cyst assemblages on the New Jersey Shelf. Biogeosciences, 6(8), 1755–1781. https://doi.org/10.5194/bg-6-1755-2009

Sluijs, Appy, & Dickens, G. R. (2012). Assessing offsets between the δ 13 C of sedimentary components and the global exogenic carbon pool across early Paleogene carbon cycle perturbations. Global Biogeochemical Cycles, 26(4), 2011GB004224. https://doi.org/10.1029/2011GB004224

Sluijs, Appy, Brinkhuis, H., Schouten, S., Bohaty, S. M., John, C. M., Zachos, J. C., et al. (2007). Environmental precursors to rapid light carbon injection at the Palaeocene/Eocene boundary. Nature, 450(7173), 1218–1221. https://doi.org/10.1038/nature06400

Sluijs, Appy, Schouten, S., Donders, T. H., Schoon, P. L., Röhl, U., Reichart, G.-J., et al. (2009). Warm and wet conditions in the Arctic region during Eocene Thermal Maximum 2. Nature Geoscience, 2(11), 777–780. https://doi.org/10.1038/ngeo668

Sluijs, Appy, van Roij, L., Frieling, J., Laks, J., & Reichart, G.-J. (2018). Single-species dinoflagellate cyst carbon isotope ecology across the Paleocene-Eocene Thermal Maximum. Geology, 46(1), 79–82. https://doi.org/10.1130/G39598.1

Stockmarr, J. (1972). Tablets with spores used in absolute pollen analysis,. Pollen Spores, 13, 615–621.

Svensen, H., Planke, S., Malthe-Sørenssen, A., Jamtveit, B., Myklebust, R., Rasmussen Eidem, T., & Rey, S. S. (2004). Release of methane from a volcanic basin as a mechanism for initial Eocene global warming. Nature, 429(6991), 542–545. https://doi.org/10.1038/nature02566

Taylor, K. W. R., Huber, M., Hollis, C. J., Hernandez-Sanchez, M. T., & Pancost, R. D. (2013). Re-evaluating modern and Palaeogene GDGT distributions: Implications for SST reconstructions. Global and Planetary Change, 108, 158–174. https://doi.org/10.1016/j.gloplacha.2013.06.011

Thöle, L. M., Nooteboom, P. D., Hou, S., Wang, R., Nie, S., Michel, E., et al. (2023). An expanded database of Southern Hemisphere surface sediment dinoflagellate cyst assemblages and their oceanographic affinities. Journal of Micropalaeontology, 42(1), 35–56. https://doi.org/10.5194/jm-42-35-2023

Thomas, E., & Zachos, J. C. (2000). Was the late Paleocene thermal maximum a unique event? GFF, 122(1), 169–170. https://doi.org/10.1080/11035890001221169

Tierney, J. E., Zhu, J., Li, M., Ridgwell, A., Hakim, G. J., Poulsen, C. J., et al. (2022). Spatial patterns of climate change across the Paleocene–Eocene Thermal Maximum. Proceedings of the National Academy of Sciences, 119(42), e2205326119. https://doi.org/10.1073/pnas.2205326119

Torsvik, T. H., Van der Voo, R., Preeden, U., Mac Niocaill, C., Steinberger, B., Doubrovine, P. V., et al. (2012). Phanerozoic polar wander, palaeogeography and dynamics. Earth-Science Reviews, 114(3–4), 325–368. https://doi.org/10.1016/j.earscirev.2012.06.007

Tuenter, E., Weber, S. L., Hilgen, F. J., & Lourens, L. J. (2003). The response of the African summer monsoon to remote and local forcing due to precession and obliquity. Global and Planetary Change, 36(4), 219–235. https://doi.org/10.1016/S0921-8181(02)00196-0

Usup, G., Ahmad, A., Matsuoka, K., Lim, P. T., & Leaw, C. P. (2012). Biology, ecology and bloom dynamics of the toxic marine dinoflagellate Pyrodinium bahamense. Harmful Algae, 14, 301–312. https://doi.org/10.1016/j.hal.2011.10.026

Vallé, F., Westerhold, T., & Dupont, L. M. (2017). Orbital-driven environmental changes recorded at ODP Site 959 (eastern equatorial Atlantic) from the Late Miocene to the Early Pleistocene. International Journal of Earth Sciences, 106(3), 1161–1174. https://doi.org/10.1007/s00531-016-1350-z

Wagner, T. (2002). Late Cretaceous to early Quaternary organic sedimentation in the eastern Equatorial Atlantic. Palaeogeography, Palaeoclimatology, Palaeoecology, 179(1–2), 113–147. https://doi.org/10.1016/S0031-0182(01)00415-1

Weedon, G. P., Shackleton, N. J., & Pearson, P. N. (Eds.). (1997). The Oligocene time scale and cyclostratigraphy on the Ceara Rise, Western Equatorial Atlantic (Vol. 154). Ocean Drilling Program. https://doi.org/10.2973/odp.proc.sr.154.1997

van der Weijst, C. M. H., van der Laan, K. J., Peterse, F., Reichart, G.-J., Sangiorgi, F., Schouten, S., et al. (2022). A 15-million-year surface- and subsurface-integrated TEX86 temperature record from the eastern equatorial Atlantic. Climate of the Past, 18(8), 1947–1962. https://doi.org/10.5194/cp-18-1947-2022

Westerhold, T., Röhl, U., Pälike, H., Wilkens, R., Wilson, P. A., & Acton, G. (2014). Orbitally tuned timescale and astronomical forcing in the middle Eocene to early Oligocene. Climate of the Past, 10(3), 955–973. https://doi.org/10.5194/cp-10-955-2014

Westerhold, T., Röhl, U., Donner, B., & Zachos, J. C. (2018). Global Extent of Early Eocene Hyperthermal Events: A New Pacific Benthic Foraminiferal Isotope Record From Shatsky Rise (ODP Site 1209). Paleoceanography and Paleoclimatology, 33(6), 626–642. https://doi.org/10.1029/2017PA003306

Westerhold, Thomas, Röhl, U., Frederichs, T., Agnini, C., Raffi, I., Zachos, J. C., & Wilkens, R. H. (2017). Astronomical calibration of the Ypresian timescale: implications for seafloor spreading rates and the chaotic behavior of the solar system? Climate of the Past, 13(9), 1129–1152. https://doi.org/10.5194/cp-13-1129-2017

Westerhold, Thomas, Marwan, N., Drury, A. J., Liebrand, D., Agnini, C., Anagnostou, E., et al. (2020). An astronomically dated record of Earth's climate and its predictability over the last 66 million years. Science, 369(6509), 1383–1387. https://doi.org/10.1126/science.aba6853

Willard, D. A., Donders, T. H., Reichgelt, T., Greenwood, D. R., Sangiorgi, F., Peterse, F., et al. (2019). Arctic vegetation, temperature, and hydrology during Early Eocene transient global

warming events. Global and Planetary Change, 178, 139–152. https://doi.org/10.1016/j.gloplacha.2019.04.012

Wubben, E., Veenstra, T., Witkowski, J., Raffi, I., Hilgen, F., Bos, R., et al. (2023). Astrochronology of the Miocene Climatic Optimum record from Ocean Drilling Program Site 959 in the eastern equatorial Atlantic. Newsletters on Stratigraphy. https://doi.org/10.1127/nos/2023/0749

Wubben, E., Spiering, B. R., Veenstra, T. J. T., Bos, R., Wang, Z., Dijk, J. V., et al. (in press). Tropical Warming and Intensification of the West African Monsoon during the Miocene Climatic Optimum (preprint). Preprints. https://doi.org/10.22541/essoar.169603553.36604170/v1.

Zachos, J. C., McCarren, H., Murphy, B., Röhl, U., & Westerhold, T. (2010). Tempo and scale of late Paleocene and early Eocene carbon isotope cycles: Implications for the origin of hyperthermals. Earth and Planetary Science Letters, 299(1–2), 242–249. https://doi.org/10.1016/j.epsl.2010.09.004

Zeeden, C., Hilgen, F., Röhl, U., Seelos, K., & Lourens, L. (2015). Sediment color as a tool in cyclostratigraphy – a new application for improved data acquisition and correction from drill cores. Newsletters on Stratigraphy, 48(3), 277–285. https://doi.org/10.1127/nos/2015/0064

Zhang, Y., Boer, A. M., Lunt, D. J., Hutchinson, D. K., Ross, P., Flierdt, T., et al. (2022). Early Eocene Ocean Meridional Overturning Circulation: The Roles of Atmospheric Forcing and Strait Geometry. Paleoceanography and Paleoclimatology, 37(3), e2021PA004329. https://doi.org/10.1029/2021PA004329

Zonneveld, K. A. F., Marret, F., Versteegh, G. J. M., Bogus, K., Bonnet, S., Bouimetarhan, I., et al. (2013). Atlas of modern dinoflagellate cyst distribution based on 2405 data points. Review of Palaeobotany and Palynology, 191, 1–197. https://doi.org/10.1016/j.revpalbo.2012.08.003